Density waves in gravity-driven granular flow through a channel

Elizabeth D. Liss, Stephen L. Conway, and Benjamin J. Glasser[a)]
Department of Chemical and Biochemical Engineering, Rutgers University, Piscataway, New Jersey 08854

(Received 26 July 2001; accepted 17 June 2002; published 6 August 2002)

A molecular-dynamic computer simulation is used to examine rapid granular flow in a vertical channel. A two-dimensional event driven algorithm is used with periodic boundary conditions in the flow direction and solid walls in the lateral direction. Flow in the channel leads to an inhomogeneous distribution of the particles and two distinct types of density waves are identified: An S-shaped wave and a clump. The density waves are further characterized by quantifying their temporal evolution using Fourier methods and examining local and global flow properties of the system, including velocities, mass fluxes, granular temperatures, and stresses. A parametric study is used to characterize the effect of the system parameters on the density waves. In particular we are able to show that the dynamics of large systems are often qualitatively and quantitatively different from those of small systems. Finally, the types of density waves and dominant Fourier modes observed in our work are compared to those that are predicted using a linear stability analysis of equations of motion for rapid granular flow.
[DOI: 10.1063/1.1499126]

I. INTRODUCTION

Although the transport of bulk solid materials is an integral part of many industrial processes, a fundamental understanding of granular flows is far from complete. The flow of granular material has been seen to exhibit many complexities including normal stress differences, heap formation, convection under vibration and density inhomogeneities.[1–6] There has recently been a significant amount of interest in understanding the formation of density waves and their effect on rapid granular flows. Because of the complex behavior of granular flows, researchers have generally focused on geometrically simple flow situations. Such work includes flow in shear cells, inclined chutes and vertical channels and various types of density waves have been observed in all of these systems.[3,7–14] Density waves may affect the flow properties, heat transfer, and reaction rates of a process involving granular materials.[15] In addition, an understanding of the rapid flow of a granular material ties in directly with an understanding of many gas–particle flows.[16–19] In general, gas–particle interactions as well as particle–particle and particle–wall interactions can lead to the formation of density waves in gas–particle flows. In this work we are interested in characterizing and examining the effect of density waves in rapid granular flow in a vertical channel.

Molecular or particle dynamic simulations have become an integral tool in investigating granular flows.[20–22] Such simulations are very powerful tools because, in principle, they are able to give one all the information about the system.[19,23,24] One is able to obtain local information on flow and stresses that are difficult if not currently impossible to obtain experimentally. Particle dynamic[25–27] and lattice-gas-automata simulations[28] have identified density waves in gravity driven granular flows. Poschel[27] conducted two-dimensional molecular-dynamic simulations of flow through a narrow vertical pipe and found that even if the flow is initially uniform, density waves become apparent. Peng and Herrmann[28] used a lattice-gas-automata simulation to examine density waves and found that inelastic collisions between particles and rough walls were necessary for the formation of these waves. A parametric investigation of the types of density waves that form and an examination of the effect of the inhomogeneities on the global flow properties of granular materials have been left incomplete.

In addition to simulations, continuum theories have been developed to investigate granular flow in channels. Density waves in gravity-driven granular flows in a vertical channel have been studied using a variety of techniques including modeling the system as interacting kinetic waves,[26] using the Langevin equation,[29] and using the kinetic theory of dissipative gasses.[30,31] Wang, Jackson, and Sundaresan[30] conducted a linear stability analysis of equations of motion for granular materials[32] for three-dimensional gravity flow between parallel walls. They found that the base state was unstable to perturbations in the form of density waves. Eigenfunctions corresponding to the unstable modes were examined and it was observed that three basic structures could be identified. Wang and Tong[33] examined the temporal evolution of these three instability modes through numerical simulation and Fourier analysis. Valance and Le Pennec[31] connected density waves in vertical channel flow to dynamical instabilities by conducting a linear and nonlinear analysis of quasi-one-dimensional equations of motion for granular materials. They found that below a critical value of flow density the flow destabilizes and density waves form.

On earth an interstitial fluid, such as air, is usually present and depending on the specific flow situation the hy-

[a)]Author to whom correspondence should be addressed. Telephone: 732-445-4243; fax: 732-445-2581. Electronic mail: bglasser@sol.rutgers.edu

drodynamic forces due to the interstitial fluid (air) may have a significant effect on the flow of grains. The role that the interstitial fluid has in the formation of density waves in vertical channels has been a subject of investigation. Much of the recent experimental work done on gravity flows of granular material in pipes has examined the different flow regimes found in narrow pipes.[26,28,34–38] Horikawa *et al.*[34] hypothesized that back flow of gas is necessary for the formation of density waves. These results and the theoretical and computational investigations that are able to predict the formation of density waves without considering the presence of air, question the relative importance of the mechanisms proposed for the formation of density waves. To gain a complete understanding of gas–solid flows one must take into account both the effects of gas–solid interactions as well as particle–particle interactions. Models of gas–solid flows often contain separate terms to model forces due to gas–particle and due to particle–particle interactions.[39] If inhomogeneities occur it is important to understand the effect of inhomogeneities on both of these terms. This work will investigate the effect of inhomogeneities on the particle–particle contribution to the stress tensor.

The structure of this paper is as follows. In Sec. II the computer simulation used for this study will be described. In Sec. III the density waves we have observed will be characterized. Two distinct types of density waves are identified and the effect of system parameters on the type of wave that forms is examined. The temporal evolution of the waves is examined using Fourier methods. This is followed by a discussion of the effect of the density waves on characteristic flow properties. Section IV offers a comparison with theoretical predictions and Sec. V a summary of the results.

II. COMPUTER SIMULATION

The system studied in this work consists of N identical rigid disks of equal mass and diameter d enclosed in a rectangular cell of length L and width W (see Fig. 1). The system is enclosed with solids walls in the lateral (y) direction and is periodically extended in the vertical (x) direction. This two-dimensional system of disks can be interpreted as a three-dimensional system with the motion of the spheres (of appropriate mass) confined to the $x-y$ plane of interest. In this work we have simulated the rapid flow regime where it is assumed that collisions between particles are binary and instantaneous and that the particles act as hard disks. We have adopted an event driven algorithm, which is computationally efficient for the rapid flow regime.[7]

The only interactions that are allowed are instantaneous contacts between pairs of particles and between a particle and a wall. The lateral component of velocity of each disk remains constant between collisions and the vertical component of the velocity increases due to the gravitational force. When the disks impact they lose energy due to the fact that the collisions are inelastic. The determination of the post-collision velocity is determined by conservation of linear momentum together with the additional information provided by the restitution of the particle. Conservation of linear momentum can be written in the following form:

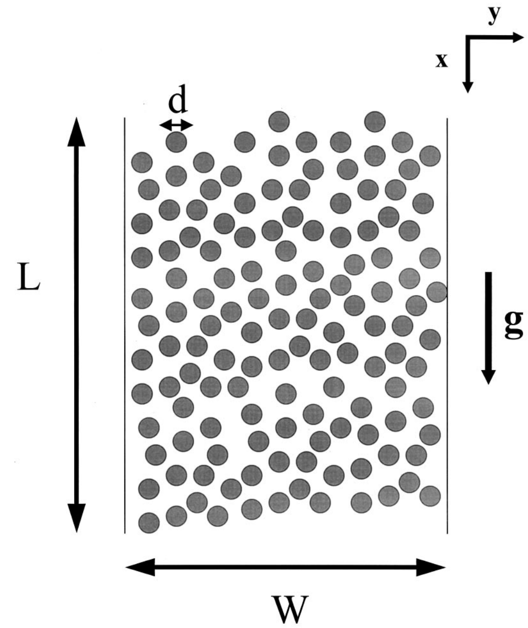

FIG. 1. Schematic of gravity-driven flow in a channel.

$$m_1\boldsymbol{c}_1+m_2\boldsymbol{c}_2=m_1\boldsymbol{c}_1'+m_2\boldsymbol{c}_2', \tag{1}$$

where m_i is the mass of the ith particle, $\boldsymbol{c}_i$ is the translational velocity of the particle and primed quantities indicates post-collisional quantities. The degree of inelasticity is reflected in the coefficient of normal restitution, e_p, which is the ratio of the post-collisional and pre-collision velocities normal to the particle–particle surface contact. This information takes the following form:

$$e_p=\frac{-\boldsymbol{k}\cdot\boldsymbol{w}_{12}'}{\boldsymbol{k}\cdot\boldsymbol{w}_{12}}, \tag{2}$$

where $\boldsymbol{w}_{12}=\boldsymbol{c}_1-\boldsymbol{c}_2$ is the relative velocity of the colliding particles, $\boldsymbol{k}$ is the unit vector along the line from the center of particle 1 to the center of particle 2 and is given by

$$\boldsymbol{k}=\frac{(\boldsymbol{x}_1-\boldsymbol{x}_2)}{\|\boldsymbol{x}_1-\boldsymbol{x}_2\|}, \tag{3}$$

where $\boldsymbol{x}_i$ is the position of the ith particle.

The relative tangential velocities after a particle–particle collision are based on the surface friction. Surface friction for particle interactions is modeled by incorporating a tangential coefficient of restitution, β, which is equal to the ratio of the final to initial relative tangential velocities at the point of contact.[2,40] The tangential coefficient of restitution is given by the following relationship:[40]

$$\boldsymbol{k}\times\boldsymbol{g}_{12}'=-\beta(\boldsymbol{k}\times\boldsymbol{g}_{12}), \tag{4}$$

where

$$\boldsymbol{g}_{12}=\boldsymbol{c}_{12}-\frac{d}{2}\boldsymbol{k}\times(\omega_1+\omega_2),$$

and d and ω_i are, respectively, the diameter and angular velocity of the (ith) particle.

The effect of particle friction can be examined by varying the value of β chosen. The parameter β was initially set equal to -1, which results in the tangential components of the velocity to remain unchanged upon particle–particle impact. This case will allow for a direct comparison with previous continuum work on this system. The situation of fully rough particles was also examined by setting β equal to 0, which makes the surface friction of the particles large enough to stop any relative tangential motion of the particles upon impact. Intermediate cases were also examined in order to ascertain the effect of particle friction on the results (see Sec. III A).

The solid boundaries are modeled as frictional surfaces and a particle impacting with a wall is analogous to a particle colliding with a particle of infinite mass moving at the velocity of the wall. A unique coefficient of normal restitution, e_w, is defined for collisions between particles and a wall. The frictional properties of the walls were modeled in two different ways. The first involved the use of a specularity coefficient, ϕ', which is defined as the average fraction of relative tangential momentum transmitted from a particle to the wall during impact.[41] The second involved the use of a unique coefficient of tangential restitution, β_w for collisions between particles and a wall.[40] This model has been implemented by a large number of researchers carrying out particle dynamic simulations.[2] By varying β_w or ϕ' the effect of wall boundary conditions could be examined. The first model (i.e., a specularity coefficient) was chosen because it will allow for a direct comparison with a continuum analysis of this system, which will be discussed in Sec. IV. Defining a specularity coefficient is equivalent to defining a tangential coefficient of restitution for stationary walls. The effect of wall friction can be examined by varying the value of ϕ' chosen. A value of $\phi'=0$ corresponds to a fully rough wall (i.e., after a collision there is no relative tangential slip between the particle–surface and the wall) while nonzero values allow for tangential slip.

Two initial conditions are used in this work. The first is a homogeneous initial condition and is a gas of initial uniform macroscopic density, which corresponds to an elastic hard disk gas with zero average velocity.[12] The configuration is achieved by first distributing disks uniformly within the enclosure and then assigning the disks velocities drawn from a Gaussian distribution with a zero mean and a variance that corresponds to the initial granular temperature. The second initial condition is a plug of material in the center of the channel. This condition corresponds to the fully developed flow that is observed in small channels and thus in some sense represents a base state flow solution (see Sec. III A for further details). This initial condition will allow for a direct comparison with previous continuum work on channel flow. From these initial states the simulation is allowed to evolve. In many granular flows it has been shown that as the system evolves, from an initial uniform condition, the global properties of the system, including stress, change significantly until the system reaches a statistical steady state.[11] A similar behavior is observed for gravity driven flow in a channel. Once the statistical steady state has been achieved, representative macroscopic quantities were calculated. The development of steady flow regimes and the behavior of the system once it has reached a statistical steady state will be examined in Sec. III A.

The program only searches for collisions between particles that are located near each other, which is accomplished by sectioning the system into cells. Only the particles that are found in either the same or neighboring cells are examined for collisions.[42] The enhanced computational speed is necessary to perform simulations of large systems for long times, which are needed because the dynamics of large systems are quantitatively (and sometimes qualitatively) different from those of small systems. The difference arises due to the fact that density inhomogeneities that form in small systems can be different from those that form in larger systems. The effect of the different types of inhomogeneities on the flow will be examined by considering system properties such as stresses and granular temperature.

Transfer of microscopic momentum leads to the continuum stresses in the system. The total stress experienced by a flowing granular material is the sum of a kinetic and a collisional stress. The kinetic stress tensor is given by[20]

$$\tau^k=\rho_p \nu \langle \boldsymbol{u}' \boldsymbol{u}' \rangle, \tag{5}$$

where $\boldsymbol{u}'$ is the instantaneous deviation from the mean velocity, ρ_p is the particle density, ν is the solids fraction, and $\langle\ \rangle$ represents an average over all particles in a particular cell. The collisional stress tensor can be written as[20]

$$\tau^c=d f_c \langle \boldsymbol{J}\boldsymbol{k} \rangle, \tag{6}$$

where d is the particle diameter, f_c is the area (or volumetric) collision frequency. $\boldsymbol{J}$ is the impulse that is transferred between the two particles over a distance equal to the particle diameter. It is equal to the magnitude of the change in momentum of the colliding particles and is given by the following equation:[43]

$$\boldsymbol{J}=\frac{m}{2}(1+e_p)(\boldsymbol{g}_{12}\cdot\boldsymbol{k})\boldsymbol{k}+\frac{m}{2}\frac{(1+\beta)}{(1+K)}K(\boldsymbol{g}_{12}-(\boldsymbol{k}\cdot\boldsymbol{g}_{12})\boldsymbol{k}), \tag{7}$$

where m is the mass of a particle and K is a parameter which describes the spatial distribution of the mass and is given by

$$K=\frac{2I}{d^2}, \tag{8}$$

and I is the moment of inertia of the particles and is equal to $(md^2)/8$ for solid disks.

All stresses are reported in a dimensionless form and are nondimensionalized using $gW\rho_p$. An additional macroscopic value of interest is the granular temperature which is given by

$$T=\tfrac{1}{2}\langle \boldsymbol{u}' \boldsymbol{u}' \rangle. \tag{9}$$

The granular temperature is nondimensionalized using the scaling gW. The fluctuation velocities have been computed relative to average velocities in the region being examined. This is equivalent to dividing the system into cells (in both directions) and collecting statistics in these cells. The formation of density waves will lead to dense and dilute regions within the flow and the instantaneous local average velocity in a small region will in general differ from the global average values. (In any discrete system, statistical fluctuations about the average would occur, but the density waves will increase the magnitude of these velocity fluctuations.)

For the system described above the relevant dimensionless length scales are the ratio of the length to width, L/W, and the ratio of the width to the diameter of the particles, W/d. An additional parameter of interest is the solids fraction, ν. These three parameters are related by the definition of the solids (area) fraction:

$$\nu = \frac{N\pi d^2}{4WL} = \frac{N\pi}{4\,\frac{L}{W}\left(\frac{W}{d}\right)^2}. \tag{10}$$

The effect of varying each of these parameters on the flow behavior will be discussed below. Since we have used the dimensionless parameters in this work, the value of the diameter of the particles is only important relative to W. However it is convenient to define a diameter in order to compare our results with theoretical predictions; for this purpose we define $d = 1800\ \mu\text{m}$ without any loss of generality. The relevant time scale of the system is $(W/g)^{1/2}$ and the relevant mass is $\rho_p \pi (d/4)^2$. Because the particles simulated have a uniform mass and the stresses are scaled by the density, the actual value of the mass does not affect any of the results presented. All velocities reported in this work are nondimensionalized using the scaling $(gW)^{1/2}$.

III. RESULTS AND DISCUSSION

A. Characterization of the density inhomogeneities

Although much of this work is concerned with characterizing the flow regimes, we will start by examining the development of inhomogeneities from a homogeneous initial condition. Investigating the transient behavior of the flows will also contribute to our understanding of the relationship between the various forms of inhomogeneities that are identified. Figure 2 shows the development of the average kinetic energy per particle, E, vs time, t, for systems with the material properties listed in Table I and two different L/W ratios. The parameters in Table I correspond to our base case and represent a system where wall friction is modeled by a specularity coefficient. In Fig. 2, time and energy are nondimensionalized using the scaling $(W/g)^{1/2}$ and Wg, respectively. Figures 2(a) and 2(b) show that from a homogeneous initial condition of low granular temperature the energy increases as the particles speed up due to the gravitational force. As the particle velocities increase, the dissipation of energy due to (inelastic) particle–particle and particle–wall collisions also increases and eventually this leads to a plateau in the total energy. The system is considered to be at a statistical steady state once the energy of the system does not vary by more 5% of the plateau value for 500 collisions per particle. In the figure it can be seen that the plateau in energy (per particle) for $L/W = 2$ and $L/W = 4$ are not the same. This will be discussed further after examining each system in more detail. In Figs. 2(c) and 2(d) results are shown for the

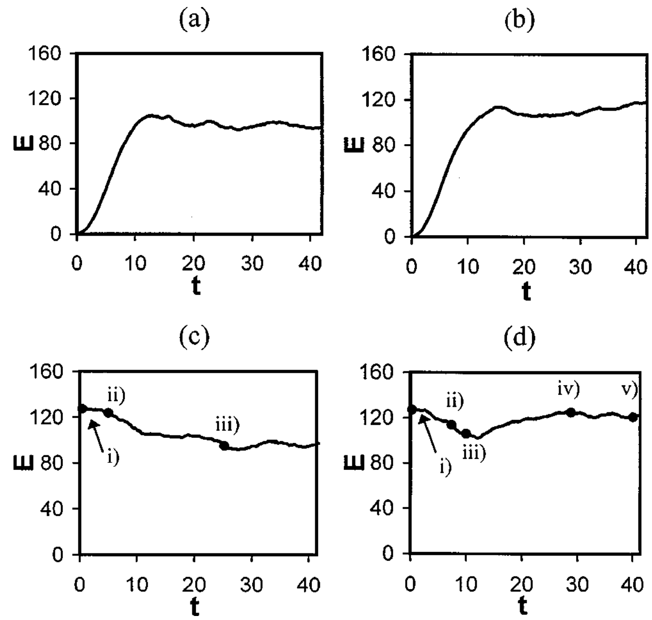

FIG. 2. Dimensionless system average energy vs dimensionless time for systems of varying size and initial conditions. $W/d = 33.3$, $\nu_{2d} = 0.31$, $e_p = 0.85$, $e_w = 0.97$, and $\phi' = 0.6$. (a) $L/W = 2$, from uniform initial condition, (b) $L/W = 4$, from uniform initial condition, (c) $L/W = 2$, from plug initial condition, (d) $L/W = 4$, from plug initial condition. (The plug initial condition was created from a simulation of an equivalent system with $L/W = 0.5$ from an initial uniform distribution. The end state was then duplicated longitudinally as necessary for larger systems and used as the new initial state.)

same parameters [as in Figs. 2(a) and 2(b), respectively] but with an initial condition corresponding to a plug of material in the center (see caption for details). Each of the simulations, respectively, reached the same plateau value of the total energy reached using the homogeneous initial condition. The fully developed flow behavior of the systems with the different initial conditions were also indistinguishable.

Simulations were carried out for different L/W values and it was observed that in each case the energy reached a plateau which corresponded to a fully developed state with an associated flow structure. Figure 3 summarizes the evolution of structure with system size and depicts the state of the systems after the simulations are considered to have reached a fully developed state. These plots represent snapshots of systems with different length but with the same average solids fraction, diameter of the particles, coefficient of restitution and width. Figure 4 shows vector plots of the flux of material for each of the systems examined in Fig. 3. The flux plots are calculated by dividing the system into cells, which contain on average three particles, and multiplying the local

TABLE I. Material properties.

Particle diameter, d:	0.0018 m
Width to diameter ratio, W/d:	33.3
Solids fraction, ν:	0.31
Particle–particle coefficient of restitution, e_p:	0.85
Tangential coefficient of restitution, β	−1
Particle–wall coefficient of restitution, e_w:	0.97
Specularity coefficient of wall collisions, ϕ':	0.6

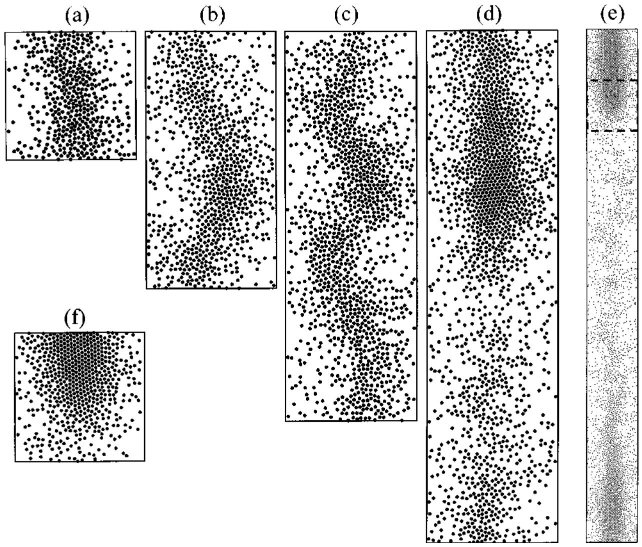

FIG. 3. Scatter plots of the position of the particles at statistical steady state for systems of varying size. $W/d=33.3$, $\nu_{2d}=0.31$, $e_p=0.85$, $e_w=0.97$, and $\phi'=0.6$. (a) $L/W=1$, (b) $L/W=2$, (c) $L/W=3$, (d) $L/W=4$, (e) $L/W=10$, (f) enlarged image of the boxed region in panel (e).

average velocity and the solids fraction within that area. The local average velocities of the particles were also examined and are dominated by the average velocity in the flow direction.

Due to the periodic boundary conditions in the vertical direction, a particle that moves out of the bottom of the periodic box will re-enter at the top. The particles are plotted as disks based on the position of their centers and thus there are particles at the top and the bottom of the system that seem to extend out of the flow domain being simulated. Figure 3(a) shows a snapshot of the system, with $L/W=1$. This snapshot was generated from a simulation that started with a homogeneous initial condition. As the simulation proceeds the particles move away from the walls and start to form a dense region in the center of the channel. As time proceeds the dense region consolidates forming into a plug flow with the maximum density and downward velocity corresponding to the center of the channel. Once the average energy of the system reaches a plateau value, the particles remain consolidated and flow as a plug. Plug flow can be defined as a flow where there is a density variation in the lateral direction (the direction perpendicular to the flow) but there is no apparent structure in the vertical direction (the direction of the flow). Even in the relatively small system, in Fig. 3(a), there is some slight variation in the vertical direction. In order to obtain a ''pure'' plug flow, which is not susceptible to slight variations in the vertical direction, even shorter systems need to be simulated. Systems as small as $L/W=0.5$ have been simulated and showed a ''pure'' plug flow.

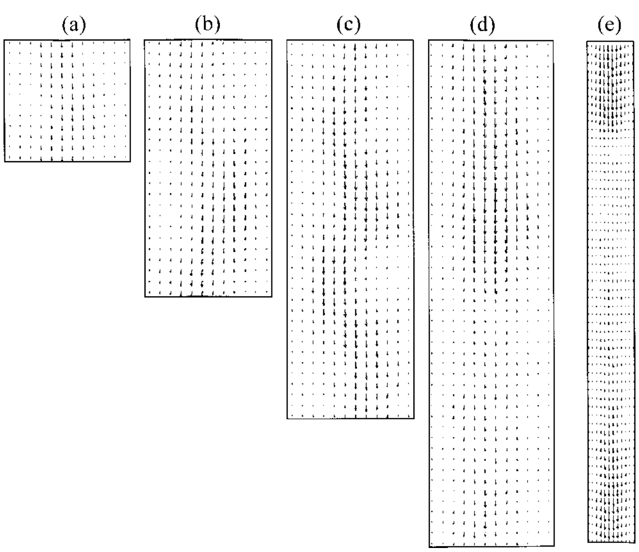

FIG. 4. Vector plot of local average flux of material for systems of varying size. $W/d=33.3$, $\nu_{2d}=0.31$, $e_p=0.85$, $e_w=0.97$, and $\phi'=0.6$ (a) $L/W=1$, (b) $L/W=2$, (c) $L/W=3$, (d) $L/W=4$, (e) $L/W=10$.

It is not surprising that a system bounded with walls should develop a plug flow since a similar structure, with a low density region near the walls and a high density plug in the center of the flow domain, has been observed in Couette flow[7,23,44–48] and gravity flow systems.[30] Plug flow has been attributed to the shear exerted by the walls on the particles.[23,45–47] In this system with $e_w=0.97$ the walls act as a source of pseudo-thermal energy and create an increase in granular temperature near the walls (see Sec. III B). The increase in granular temperature results in a decrease in solids fraction near the wall and a corresponding increase in solids fraction in the center of the flow (due to mass conservation). The exact shape of the solids fraction profile and the degree of densification in the center of a Couette flow system has been shown to depend on the system parameters W/d, ν and shear rate.[7,23,44,45,47,48] A similar observation can be made for gravity-driven flow in a vertical channel.[30] Depending on the system parameters, the gradient in solids fraction across the channel can be more or less pronounced.

It is of interest to examine the structure of the plug as system size is changed. System size is a significant parameter because many research experiments and simulations of granular materials are done for small scales while industrial processes are conducted on larger scales. Experimental systems or simulations may not capture the appropriate structure formation and therefore may not capture all the physics of a large industrial system to observe vertical structure in the flow. Figure 3(b) shows a snapshot for the fully developed state for the same physical parameters as Fig. 3(a) but with $L/W=2$. A one-humped S-shaped wave is now apparent and this structure moves through system with time. It is of interest to examine the temporal development of this wave. Figure 5 shows the evolution from a plug initial condition to a statistical steady state. The plug initial condition was created from the fully developed state for $L/W=0.5$; this state was duplicated longitudinally as necessary for the longer system. The snapshots of the system in Fig. 5 were taken consecutively in time at the points depicted as solid circles on the energy vs time plot, in Fig. 2(c). As shown in Fig. 5(a), initially (at the first point in time) the particles are distributed throughout the system in a plug. However, the plug flow is unstable and as time proceeds the total energy of the system decreases gradually and vertical density variations start to develop as shown in Fig. 5(b).

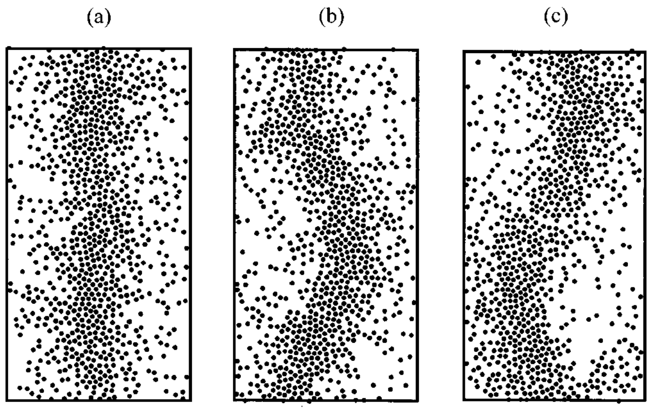

FIG. 5. Temporal development of a system with $L/W=2$, $W/d=33.3$, $\nu_{2d}=0.31$, $e_p=0.85$, $e_w=0.97$, and $\phi'=0.6$. Scatter plots of the positions of particles at dimensionless times (a) $t=0.5$, (b) $t=5$, (c) $t=25$.

The observed instability takes the form of an antisymmetric mode, i.e., a region with an increase in density has a corresponding region with a decrease in density across the system centerline. This leads to a S-shaped one-humped density wave that moves through the channel. This instability (as well as other cases) will be further characterized using a Fourier analysis in Sec. III C. The extent of vertical structure initially increases and during this period the energy gradually decreases. Once the energy reaches a plateau the wave takes on the essential features of a fully developed travelling wave, i.e., a wave that has a fixed structure and moves through bed at a constant speed. In a continuum framework, a traveling wave would appear as a steady state when viewed from a frame of reference moving at the speed of the wave. In this discrete system, fluctuations are always present and statistical variations in the total energy and structure of the wave are observed. Thus, calling the wave a "traveling wave" is perhaps not completely appropriate since there is some modulation of the wave as it moves. However, the basic one-humped structure and general features remain present for all the times we have examined (which correspond to thousands of collisions per particle). This basic structure can clearly be seen in the successive snapshots shown in Figs. 5(b) and 5(c).

By generating contour plots of these successive snapshots one can determine a velocity of the wave. For this system the dimensionless wave velocity is 8.3 ± 0.7 while the system average particle velocity is 7.0. Thus, the one-humped wave moves through the system with a velocity slightly larger than the granular material (on average). To investigate the motion of the wave we have followed specific particles through the flow. From following tracer particles it is clear that particles in the dense regions moves primarily in the vertical direction while in the dilute regions the particles have significantly more radial motion. The corresponding flux plot in Fig. 4(b) shows that most of the material transfer takes place in the high-density regions. The effect of localized high and low density regions on the overall flow will be examined in detail in Sec. III B.

The evolution of the wave from the homogeneous initial condition has also been examined and is presented elsewhere.[49] In such a case the particles are initially distributed homogeneously through the system but as time proceeds they form a dense plug in the center of the channel. This dense region consolidates, becoming more dense and narrow and develops into a plug flow where there is essentially no variation in the vertical direction. Vertical density variations then develop in the same manner as shown in Fig. 5. The same fully developed state evolves from the different initial conditions.

The transition between plug flow and a S-shaped one-humped wave has been investigated by running simulations for decreasing values of L/W values (from 2 to 1). At intermediate values of L/W the vertical instability can be observed but becomes less pronounced until $L/W=1.1$, where it is no longer obviously discernable. For larger L/W, two-humped S-shaped waves have been observed: Figure 3(c) shows a snapshot for the fully developed state for $L/W=3$. The temporal evolution of this state is analogous to that for the one-humped wave. However, in this case, the instability takes the form of a period two antisymmetric mode, which leads to a two-humped density wave. Successive snapshots for this case have been examined (see Ref. 49) and while it is clear that the dominant structure is a two-humped wave at all times, it can be seen that there is some modulation of the basic structure as the wave moves through the system. A dimensionless wave velocity was computed, as before, and it has a value of 7.0 ± 1 while the system average velocity is 6.9. Simulations performed at intermediate values of L/W show that as L/W is decreased from 3 to 2 the system can be characterized as a two-humped wave until $L/W=2.25$, where a transition state occurs. At this value of L/W the wave does not achieve a single identifiable structure but rather changes significantly as it moves down through the channel. It appears at different points in time as a one-humped wave, a two-humped wave and something in between the two.

Figure 3(d) shows a snapshot for the fully developed state for $L/W=4$—clearly, something else has developed. The temporal development of a system with $L/W=4$ is slightly more complicated than it is for smaller systems and shows the relationship between the three forms of inhomogeneities that we have observed in gravity driven flows of granular materials in a channel. Figure 6 shows the evolution from the plug initial condition to a statistical steady state for this system. (Again, this initial condition was constructed by longitudinally duplicating the fully developed state for $L/W=0.5$.) The snapshots of the system in Fig. 6 were taken consecutively in time at the points depicted as solid circles on the energy vs time plot, in Fig. 2(d). Initially (at the first point in time) the particles are distributed throughout the system in a plug as shown in Fig. 6(a). However, the plug flow is unstable and as time proceeds the total energy of the system initially decreases and the presence of a vertical instability becomes apparent [see Fig. 6(b)]. Something that resembles a perturbed three-humped wave begins to form as the energy of the system continues to decrease, goes through a minimum and then gradually increases. Even though the energy of the system appears to level off, it does not immediately reach a steady state but continues to increase slightly

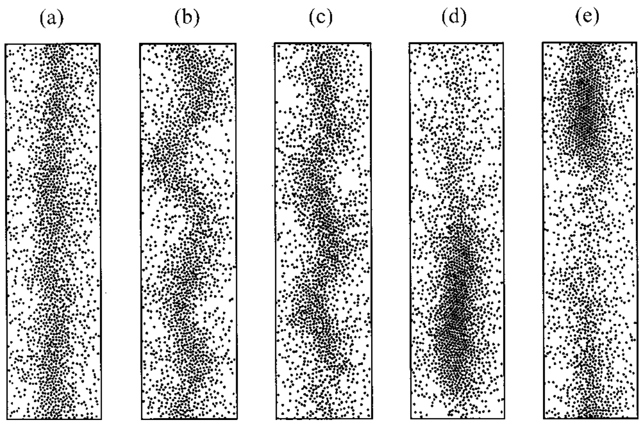

FIG. 6. Temporal development of a system with $L/W=4$, $W/d=33.3$, $\nu_{2d}=0.31$, $e_p=0.85$, $e_w=0.97$, and $\phi'=0.6$. Scatter plots of the positions of particles at dimensionless times (a) $t=2$, (b) $t=7.5$, (c) $t=10$, (d) $t=28.8$, (e) $t=40$.

with time. This is due to the fact that the structure formation in this system is not yet complete and it takes longer to reach a fully developed state. Figure 6(c) shows that a localized region of high density begins to form. Eventually, this region becomes more pronounced forming a dense clump as shown in Fig. 6(d). The clump then consolidates and remains stable over long periods of time [see Fig. 6(e)]. A Fourier analysis will be used to investigate this case in more detail in Sec. III C.

The dimensionless velocity of the clump was determined to be 9.0 ± 0.8 while the system average velocity is 7.7. The corresponding flux plot in Fig. 4(d) shows that most of the material transfer takes place in the high-density regions. We have determined the transition from a two-humped wave to a clump by examining systems with intermediate values of L/W. The transition occurs at $L/W=3.6$, where the system does not achieve a single structure but exists at different points in time as a two-humped wave, a clump or as something in between.

The above discussion shows that structure formation in simulations of gravity driven flow of granular materials in a channel can be controlled by the system size. Once a system is large enough to capture clumping, simulating a system more than twice as large does not alter the flow behavior of the material. The system shown in Fig. 3(e) with $L/W=10$ exhibits the same behavior as the system with $L/W=4$. Figure 3(f) shows an enlarged image of the region of Fig. 3(e), which is surrounded by a dashed square, and it is apparent that within the clumped region the particles are packed very densely. The particles are organized such that there is equal spacing between particles and they are aligned into layers. A similar layering phenomena has been observed in dense Couette flow simulations and can be attributed to the geometric packing constraints of the particles (that they cannot overlap each other) while undergoing shear in very dense flows.[23,50] Although one may expect to see multiple clumps in large enough systems, we saw no evidence of this in any of the systems that we simulated. Although all of the structures shown in Fig. 3 do fluctuate slightly with time, the basic features are stable over long periods of time, which is equivalent to thousands of collisions per particle.

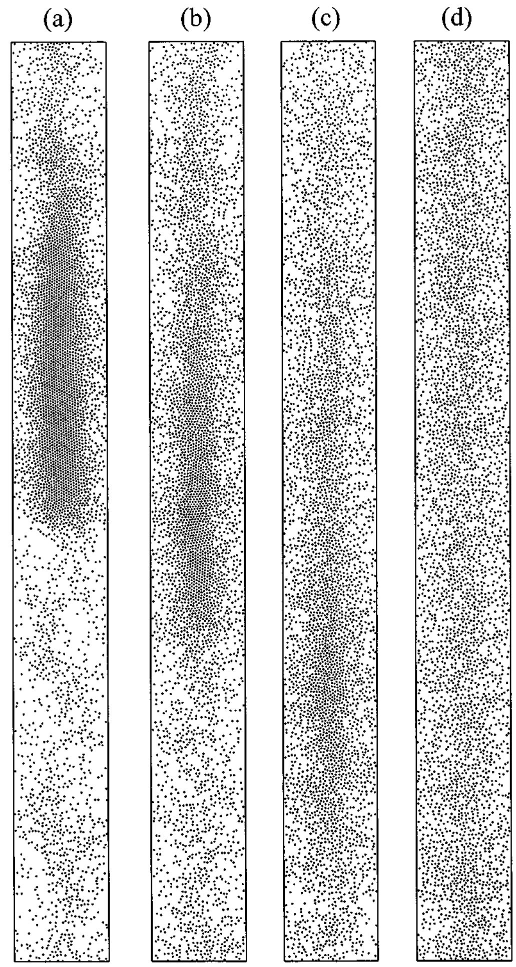

FIG. 7. Scatter plots of the position of the particles at statistical steady state for systems of varying particle–particle coefficient of restitution. $L/W=10$, $W/d=33.3$, $\nu_{2d}=0.31$, $e_w=0.97$, and $\phi'=0.6$, (a) $e_p=0.85$, (b) $e_p=0.90$, (c) $e_p=0.925$, (d) $e_p=0.95$.

Our simulations show that there are three characteristic structures that can form depending on the system parameters: A plug, a wavy flow (with period one or period two waves), and a clump. As discussed above, density wave formation has been attributed to the presence of an interstitial fluid in some cases.[34,36] Although our simulations assume that there is no fluid present in the flow, the density waves which form are similar to those observed experimentally.[27,34–37] This work confirms that density waves can form solely due to the inelastic interactions between particles and the presence of bounding walls. This is not to say that the mechanisms for the formation of density waves that can be attributed to the presence of an interstitial fluid are unimportant. In fact these mechanisms may be dominant in some cases, but it is important to understand all of the mechanisms that contribute to density wave formation.

The results discussed thus far have been for a specific set of system parameters. Robustness of the results has been examined by varying the system parameters and we have seen that the three forms of inhomogeneities defined above are robust features over a wide range of parameters. Figure 7 shows the effect of varying the particle–particle coefficient

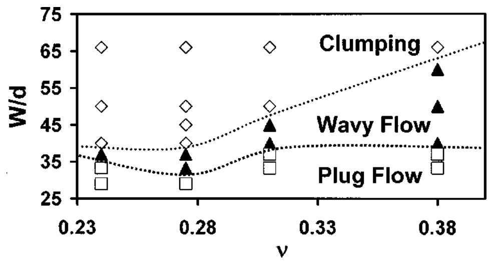

FIG. 8. Phase diagram depicting the type of inhomogeneity that is present in systems of constant size but variable solids fraction and channel width. $L/W=4$, $e_p=0.85$, $e_w=0.97$, and $\phi'=0.6$.

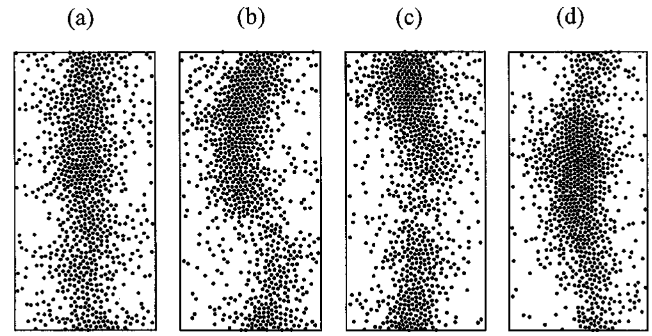

FIG. 9. Scatter plots of the position of the particles at statistical steady state for systems of varying β. $L/W=2$, $W/d=33.3$, $\beta_w=-0.4$, $\nu_{2d}=0.31$, $e_w=0.97$, and $\phi'=0.6$. (a) $\beta=-0.6$, (b) $\beta=-0.4$, (c) $\beta=-0.2$, (d) $\beta=0$.

of restitution on the fully developed inhomogeneities in a system with $L/W=10$ and the other material properties listed in Table I. It is apparent that this system is highly sensitive to e_p. Figure 7(a) shows a snapshot of the system shown in Fig. 3(e), which is characterized by a well-defined clump. As the coefficient is increased from 0.85 to 0.925 and the particles lose less energy upon collision, the clump becomes narrower and less dense [see Figs. 7(b) and 7(c)]. At a high enough e_p [see Fig. 7(d), $e_p=0.95$], the system exhibits plug flow (to a small extent). This relatively small change in the value of e_p has a significant effect on the flow behavior of the granular material. In addition, these results show that even in systems with large length to width ratios it is possible to observe stable plug flow. In contrast, simulations were performed for a particle–wall coefficient of restitution of 0.97 and 0.5. It was found that even with such a large range of values, the results were practically identical and that the value of the particle–wall coefficient of restitution had little effect on the flow and the inhomogeneities, except for a slight increase in solids fraction near the walls when $e_w=0.5$.

Wang *et al.*[30] showed, using a continuum theory, that the important system parameters for channel flow are the ratio of width to diameter of particles and the average solids fraction. Figure 8 shows a phase diagram of the effect of varying these parameters while maintaining $L/W=4$, $e_w=0.97$ and $e_p=0.85$. At low values of W/d, for the range of solids fraction examined, the system experiences plug flow. As W/d is increased, at a constant value of solids fraction, the system experiences S-shaped wavy flow at intermediate values of W/d and clumping at the highest values of W/d examined. It is apparent that as the average solids fraction is increased there is an increase in the range of W/d values for which wavy flow (the S-shaped wave) exists. Because the periodicity of the waves is dependent on L/W, only two-humped waves were observed in these simulations, with a constant value of $L/W=4$. For a given L/W value we have observed that either fully developed one-humped waves or two-humped waves can form. In addition we have observed that the two-humped waves occur in systems with higher L/W values than those with one-humped waves. It is clear from this figure that fairly modest variations in solids fraction or channel width can change the fully developed structure that is observed from a plug to a S-shaped wave to a clump. As mentioned previously, it is also possible to find states where the system does not achieve a single structure, but exists at different points in time as a two-humped wave, a clump or as something in between.

Our discussion thus far has focused on a single condition for particle–particle (β) and particle–wall friction (ϕ'). It is of interest to examine the effect of friction by considering different cases. This is particularly important because inhomogeneities are formed easily in experimental systems and the ability to observe them in a simulation should not be restricted to a specific set of speculative parameters. We carried out a large series of numerical experiments by changing the friction parameters in the model and we found the results were robust in the following sense: The three types of inhomogeneities (a plug, an S-shaped wave and a clump) discussed above were the fully developed states that were observed. The observed flow structure for a given set of parameters was fairly insensitive to the particle–wall conditions while changes in the particle–particle frictional parameter had a significant effect on the flow behavior. The effect of the wall boundary condition was investigated by first varying the specularity coefficient ϕ'. Simulations were carried out for the parameters listed in Table I but ϕ' was varied from 0.6 to 0. As discussed in Sec. II, a value of $\phi'=0$ corresponds to a fully rough wall (i.e., after a collision there is no relative tangential slip between the particle–surface and the wall) while nonzero values allow for tangential slip. It was found that even with such a large range of ϕ' values, the results were very similar, and the value of ϕ' had little effect on the fully developed inhomogeneities.

Figure 9 shows the effect of varying the particle–particle coefficient of tangential restitution, β on the steady state inhomogeneities in a system with $L/W=2$ and the other material properties listed in Table I. As discussed in Sec. II, $\beta=0$ corresponds to the fully rough case (i.e., after a collision there is no relative tangential motion of the particles) while $\beta=-1$ corresponds to the smooth case (i.e., the tangential components of the velocity to remain unchanged after particle–particle impact). In these simulations the frictional properties of the walls were modeled using a coefficient of tangential restitution, β_w for collisions between particles and the walls (see caption). Figure 9(a) shows a snapshot of the fully developed structure for a system with a particle–particle coefficient of tangential restitution of $\beta=-0.6$. For these parameters the system is characterized by a well-

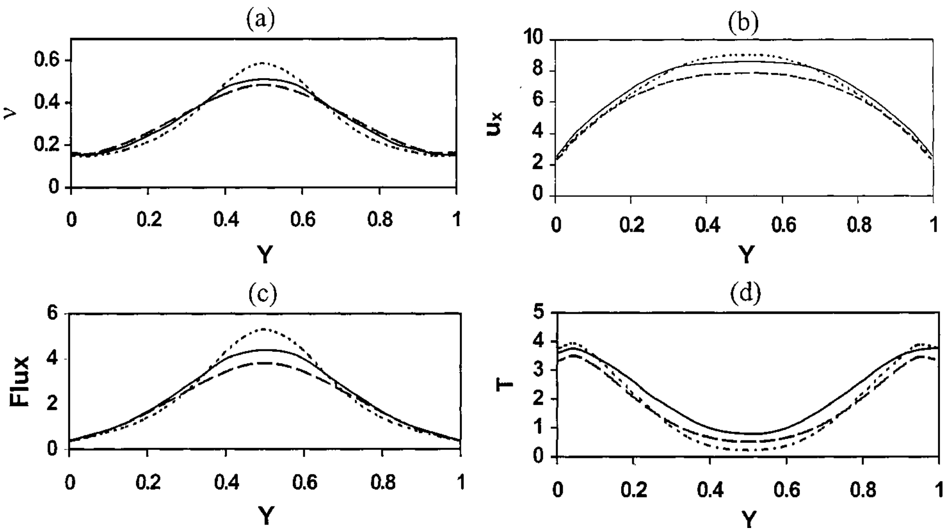

FIG. 10. Variation of long time average steady-state system properties as a function of dimensionless lateral position. $W/d=33.3$, $\nu_{2d}=0.31$, $e_p=0.85$, $e_w=0.97$, and $\phi'=0.6$. (a) Solids fraction, (b) velocity in vertical direction, (c) flux, (d) granular temperature. (· · · · $L/W=1$; — — — $L/W=2$; —— $L/W=10$.)

defined plug. As β is increased from a value of -0.6 to -0.4 the fraction of relative tangential energy lost during a collision increases and the fully developed state changes from a plug to a one-humped S-shaped wave [see Fig. 9(b)]. A further increase in β to a value of -0.2 leads to a fully developed structure that changes significantly as it moves through the channel; the wave is essentially a clump [see Fig. 9(c)] although there is marked modulation of the wave as it moves through the system. In Fig. 9(d) a snapshot is shown for a fully developed flow for $\beta=0$. The fully developed structure is similar to that for $\beta=-0.2$ and as before it changes significantly as it moves through the system. Further runs were carried out for other parameter values and the general trend that was that a fully developed plug flow could be "destabilized" by increasing the fraction of relative tangential energy lost during a collision, i.e., an increase in β could change the fully developed state from a plug flow to a wavy state. Thus, relatively small changes in the value of β had a significant effect on the flow behavior of the granular material. In contrast, simulations were carried out where the particle–wall coefficient of restitution, β_w was changed from -0.4 to 0, and the results were practically identical. Finally we reiterate, that although the quantitative details of exactly where the transition from one flow structure to the other did change, changing the frictional parameters led to the same basic inhomogeneities described above.

B. Effect of inhomogeneities on the flow properties

As defined above, flow properties such as kinetic stress, collisional stress and granular temperature are averaged quantities.[51] Typically when reporting the flow behavior of granular materials, researchers are interested in defining a single long time average over the entire system.[9,20,21] For systems that are homogeneously distributed, a single long time average value of these quantities can be appropriate. Not only is the issue of appropriate averaging important to simulations of granular flows, but it is also directly relevant to many continuum theories, which assume that there are length scales above which inhomogeneities can be ignored or averaged out (see Ref. 52). For a simple shear system the presence of clusters was determined to increase the values of the long time system averaged stresses and granular temperature.[49] In the following section we will examine how the coexistence of dense and dilute regions in the flow affects global and local system properties.

To examine the effect of density waves on the flow properties, both a single long time average and a profile of the global quantities were calculated. Figure 10 shows profiles of long time average values of the solids fraction, granular temperature, scaled velocity and flux in the x direction, as a function of dimensionless lateral position, Y. The walls are located at $Y=0$ and $Y=1$. The profiles were calculated by dividing the systems shown in Fig. 3 into strips in the lateral direction. The long time averaged solids fraction by definition remains constant in the system but the solids fraction profile changes with the form of inhomogeneity that is present. Figure 10(a) shows that when the system exists as a plug flow ($L/W=1$), the solids fraction is lower near the walls and denser in the center of the flow. When the S-shaped wavy flow is present, for $L/W=2$, the dense region is no longer constrained to the center of the pipe and the average solids fraction profile broadens slightly. For a clumped system, $L/W=10$, the particles within the clump are more densely populated than in plug flow and the solids fraction profile has a sharper peak in the center of the channel.

The single long time averaged velocity, flux, and granular temperature are also affected by structure formation. Although the velocity profiles are fairly similar for plug flow and clumping the average velocity decreases when the S-shaped wave is present [see Fig. 10(b)]. The decreased velocity directly reduces the flux of material when the system exhibits an S-shaped wave as shown in Fig. 10(c). When calculating a single system value for the flux and velocity it became apparent that these values are 10% smaller for a system with S-shaped wavy flow than one with plug flow or clumping. Examining the granular temperature emphasizes the effect of clumping on global system properties. The profile and system averaged granular temperature for plug flow and the S-shaped wavy flow are fairly similar but when a

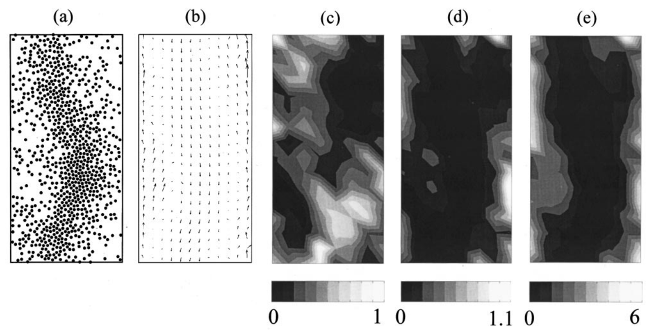

FIG. 11. Local steady-state flow properties of a system with $L/W=2$, $W/d=33.3$, $\nu_{2d}=0.31$, $e_p=0.85$, $e_w=0.97$, and $\phi'=0.6$. $M_x=16$, $M_y=8$. (a) Scatter plot of particle positions, (b) shifted local average velocity, (c) contour plot of local average collisional pressure, (d) contour plot of local average kinetic pressure, (e) contour plot of local average granular temperature.

system is clumped there is an increase in the granular temperature.

The effect of density variations on local system properties is shown in Figs. 11 and 12, which depict a one-humped wave and a clumped system, respectively. These figures show a scatter plot of the particles in the system, the local collisional and kinetic pressures, the granular temperature as well as the local velocity of the material in the system. The collisional and kinetic pressure is the sum of the normal components of the collisional and kinetic stresses, respectively. Because instantaneous values of these properties can fluctuate significantly due to the discreteness of the system,[49,53] local averages should be calculated over as much data as possible. The pressures and granular temperature were, therefore, calculated by dividing the systems into equally sized cells, which contain an average of seven particles per cell. The number of cells used in the x and y directions is M_x and M_y, respectively (see caption). An additional complication is that to accurately capture the effect of inhomogeneities, local averaging must be performed such that the position of the structure does not vary significantly over the time span of calculation. Therefore, the stresses were calculated by averaging the global properties over a period of two collisions per particle. Over this time span the wave only moves a small fraction of the flow domain.

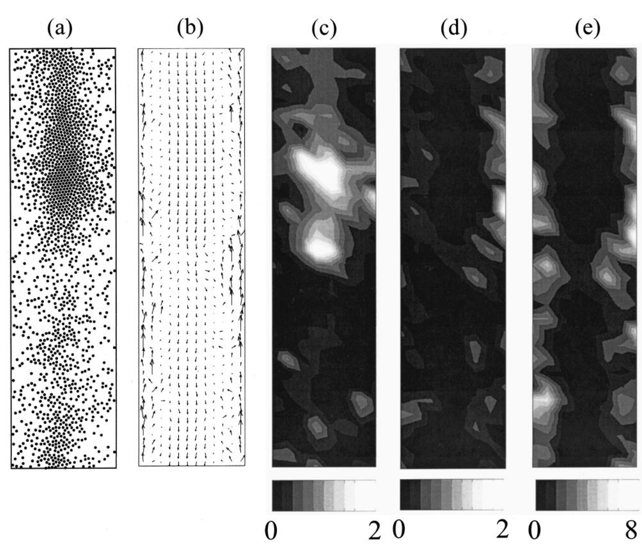

FIG. 12. Local steady-state flow properties of a system with $L/W=4$, $W/d=33.3$, $\nu_{2d}=0.31$, $e_p=0.85$, $e_w=0.97$, and $\phi'=0.6$. $M_x=32$, $M_y=8$. (a) Scatter plot of particle positions, (b) shifted local average fluctuation velocity, (c) contour plot of local average collisional pressure, (d) contour plot of local average kinetic pressure, (e) contour plot of local average granular temperature.

The local average velocity was computed by averaging the velocity of the particles in each cell. However the local average velocity is dominated by the velocity in the vertical direction for the systems in Figs. 11 and 12. (Thus a vector plot of the local average velocity shows vectors of approximately the same length pointing vertically downwards.) In order to see the variations in the local average velocity we have subtracted out the system average velocity in the flow direction. In Figs. 11(b) and 12(b) this shifted local average velocity is plotted. Since the equations describing the motion of the particles are Galilean invariant this is equivalent to viewing the system from a moving frame of reference (moving at the system average velocity). It should however be noted that the motion of the walls must also be accounted for in such a moving frame of reference, i.e., the equations are Galilean invariant only if the average velocity is also subtracted from the wall velocity. Thus if viewed from a frame of reference moving at the system average velocity then the walls would be moving at minus the system average velocity. It can be seen that the local velocities in the dense regions of a one-humped wave or a clump have a fairly constant magnitude. In addition one can easily discern that the motion of the material follows the path of the wave or clump. In contrast, the velocities in the dilute regions have a larger range of values and have relatively large magnitudes in the radial direction. The vectors describing the material adjacent to the walls are pointing upward because this material moves significantly slower than the bulk and thus the vertical value relative to the vertical system average velocity is negative. [Alternatively, in a frame of reference moving at the system average velocity, the walls would be moving upwards (not shown).]

The local collisional pressure values in both Figs. 11(c) and 12(c) vary by more than an order of magnitude over the flow domain. It is apparent from these figures that the collisional pressure is highest in the dense regions. The increase of collisional stress in the denser regions is caused by the particles in those areas having a shorter mean free path and colliding more frequently than if the particles were homogeneously distributed. In addition the reverse is true; material in the more dilute regions has a larger mean free path and thus collides less frequently resulting in a reduced collisional pressure. It is important to note that the range of values of collisional pressure is twice as large for the clumped system than for the one-humped wave, which indicates that the larger, clumped system, can experience more extreme pressures than the smaller, one-humped wave system.

The kinetic pressure and granular temperature can be seen in Figs. 11 and 12. As shown in Eqs. (5) the local fluctuation velocity directly affects the kinetic pressure. In these plots both the kinetic pressure and the granular temperature are lowest in the dense regions where the one-humped wave or clump is present. The low values of these quantities are due to the fact that the fluctuation velocity of the particles in these regions is fairly constant. Near the walls and in the more dilute regions of the system there is a larger range of velocities and the kinetic pressure and granular temperature are larger.

From Figs. 12(d) and 12(e) it becomes apparent that not only are the granular temperature and kinetic stresses lowest in the region of the clump but there is a region directly below the clump where the granular temperature is the greatest. This is due to the fact that the largest gradient in velocities is directly below the clump. Once again the range of values of kinetic pressure and granular temperature are significantly larger for the clumped system than for a one-humped wave, indicating that the larger, clumped system, can experience more extreme conditions than the smaller, one-humped wave system. Such data was also examined for a plug and two-humped wave and the same qualitative features were discerned, although the range of values in the plug was somewhat smaller.

In order to quantify (and further examine) the observation that the clumped system exhibited the largest range in the stresses we have computed stress distributions. In particular, we have examined the distribution of the values of the stresses for the clumped system and compared this to results for a plug flow. For the distributions reported in this work, local stresses were calculated by examining equally sized cells within the simulated domain that contained, on average, 14 particles. The number of cells used in the x and y directions is M_x and M_y, respectively (see caption). These values were chosen to keep the size (and aspect ratio) of the cells the same for the different systems. The stresses were then calculated in each cell over a time span of two collisions per particle. In order to collect better statistics this procedure was carried out as the system advanced in time, i.e., the local stresses were measured in time windows of two collisions per particle. The distribution of all these values in time was then determined. Choosing the value of temporal averaging as two collisions per particle was done to maximize the amount of averaging in a length of time that did not allow significant motion of the structure being examined. Results for a smaller amount of time or smaller cells gave the basic features discussed below.

The frequency distributions of the kinetic stress and collisional stresses for simulations with the material properties listed in Table I and $L/W=1$ and 4, are shown in Fig. 13. The frequency distributions are based on stresses measured in cells at a single y-location in each of the flows (see caption). It can be seen that all the distributions are positively skewed. In Figs. 13(a)–13(c) the collisional stress distributions are plotted and both the plug flow and clumped systems have similar shapes. In Figs. 13(d)–13(f) the kinetic stress distributions are plotted and as before, the plug flow and clumped systems have similar shapes. It should be noted that the τ_{xx} and τ_{yy} components of the kinetic and collisional stresses are always positive as they involve squaring the velocity or impulse components [see Eqs. (5) and (6)]. This is not the case for τ_{xy} where both negative and positive values

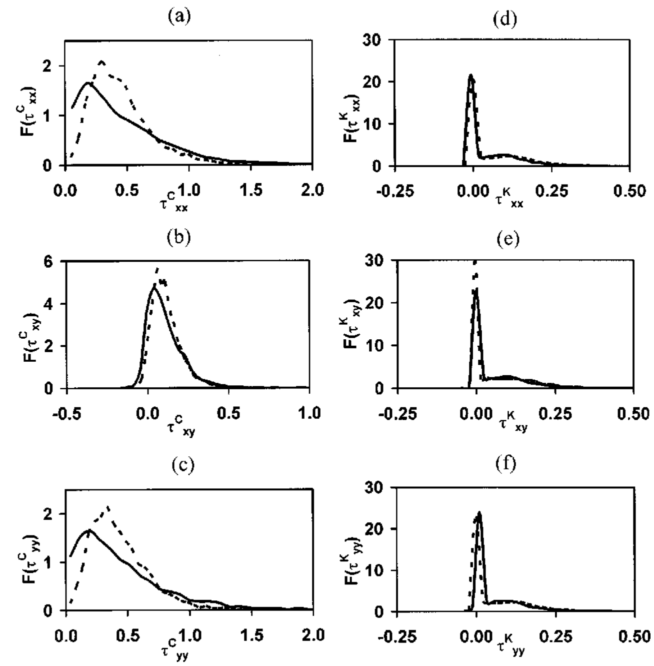

FIG. 13. Frequency distribution of the stress tensor of a system with $W/d=33.3$, $\nu_{2d}=0.31$, $e_p=0.85$, $e_w=0.97$, and $\phi'=0.6$. (a) τ^c_{xx}, (b) τ^c_{xy}, (c) τ^c_{yy}, (d) τ^k_{xx}, (e) τ^k_{xy}, (f) τ^k_{yy} ($\cdot\ \cdot\ \cdot\ \cdot$ $L/W=1$, —— $L/W=4$). For $L/W=1$, $M_x=4$, $M_y=8$; for $L/W=4$, $M_x=16$, $M_y=8$. The cells used to measure the stresses were centered at $y=0.6875$ W.

are observed. In all cases considered, the collisional stress distributions for the clumped system have a greater frequency of the largest and smallest values than the system experiencing plug flow. The increased frequency of the largest values is represented by the longer tail of the distributions, which is more apparent for τ_{xx} and τ_{yy}. There are less marked differences between the kinetic stress distributions for the plug flow and clumped system. In particular the differences are mostly quite small and thus it is not as easy to ascribe a general trend to the data. However, we can say that in all cases the frequency of the largest and smallest values for the clumped system are greater than or equal to that for the plug flow. Distributions were also computed for cells at different y-locations in the flow (not shown) and the same general trends (discussed above) were observed.

The increase of frequency of the smallest and largest values of the stresses for a clumped system can be attributed to the large variation in local particle densities that exists when this type of inhomogeneity is present. As shown in Fig. 3 the clumped systems are characterized by a region of very high solids fraction surrounded by dilute regions. The most densely populated regions of the clumped system experience a much greater number of collisions per unit time than any region of the system with plug flow, resulting in higher values of the collisional stress. Although the percentage of very high values of the stress may not be large, they can still have significant impact on the system. For example, when considering particle attrition the largest values of collisional stress controls the amount of particle breakage which occurs.[53] The increase in the frequency of the largest and smallest values of the kinetic stress in a clumped simulation can also be attrib-

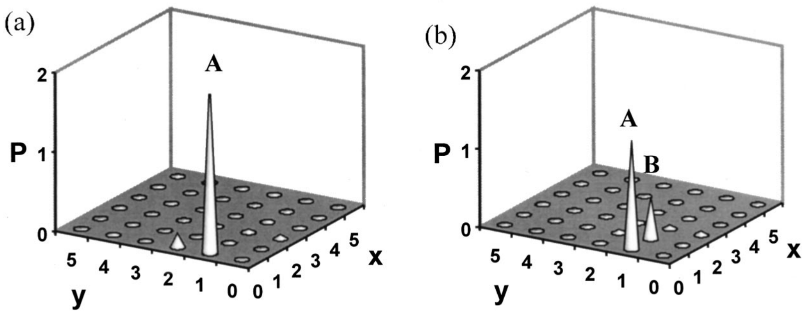

FIG. 14. Power spectrum density, P, of the transition from plug flow to a one-humped wave for a system with $L/W=2$, $W/d=33.3$, $\nu_{2d}=0.31$, $e_p=0.85$, $e_w=0.97$, $\phi'=0.6$, $N_1=24$, and $N_2=12$. Cone plots of power spectrum at dimensionless times (a) $t=0.5$, (b) $t=5$. Corresponds to Figs. 5(a) and 5(b).

uted to the diverse environment present in a clumped system. The uniform velocity of the particles on the clump, shown in Fig. 12(b), results in lower kinetic stresses in that region. In addition, the interaction between regions of high and low density in a clumped simulation results in high fluctuation velocities and thus high values of the kinetic stress.

C. Temporal evolution of flow regimes

In order to quantify the instability modes and examine the development of the different flow regimes, we have carried out a Fourier analysis of the density fields. Hopkins and Louge[9] and Wang and Tong[33,54] investigated density inhomogeneities in granular flows using a fast Fourier transform (FFT). In the former work, structure was correlated with the magnitude of the total stresses in the flow, while in the latter cases Fourier methods were used to track density wave formation. A similar Fourier analysis is used here to examine the development of the wavy and clump flow regimes in the spatial domain, by monitoring dominant frequencies in wave number space.

A two-dimensional FFT is used to quantify the amplitude of density fluctuations. As described in the previous section, density fields were generated by dividing the system into cells, resulting in an even distribution of $N_1 \times N_2$ data points in the space domain, where the subscripts refer to the x and y coordinates, respectively. The FFT algorithm in MATLAB is used to generate an N_1 by N_2 matrix of (generally) complex Fourier expansion coefficients, $\mathbf{X}$. The dimensions of $\mathbf{X}$ were set to exactly match the density data set dimensions to avoid automatic truncation or addition of zero values by the MATLAB algorithm. This avoids generation of sharp discontinuities, which would lead to false Fourier coefficients adjacent to the true values, trailing off as $1/N$. The complex Fourier coefficients were used to compute power spectra, and here the values of the power matrix, $\mathbf{P}$, are calculated using

$$\mathbf{P}=\frac{2\cdot\mathbf{X}\cdot\mathrm{conj}(\mathbf{X})}{(N_1N_2)^2}. \tag{11}$$

This form of the power function is normalized by the (squared) denominator value, to remove the dependence of power on the mesh size chosen. Power spectra, $\mathbf{P}$, for the Fourier transforms of the density fields are depicted as surface plots (which are shown in Figs. 14–16), where peak amplitudes correspond to $|a_{j,k}|$ in the general Fourier series term $a_{j,k}\exp[i2\pi((b_jx/L)+(b_ky/W))]$ (where $a_{j,k}$ is com-

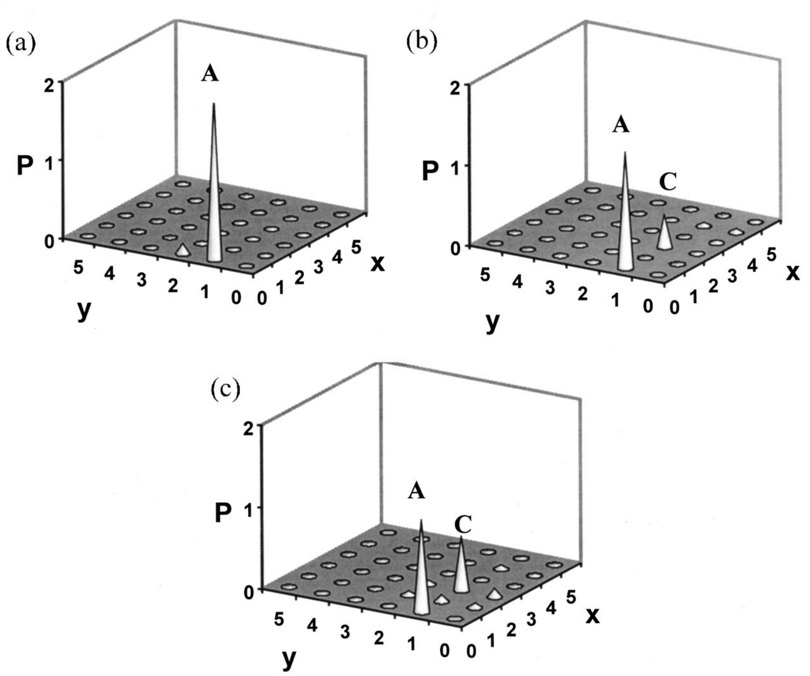

FIG. 15. Power spectrum density, P, of the transition from plug flow to a two-humped wave for a system with $L/W=3$, $W/d=33.3$, $\nu_{2d}=0.31$, $e_p=0.85$, $e_w=0.97$, $\phi'=0.6$, $N_1=36$, and $N_2=12$. Cone plots of power spectrum at dimensionless times (a) $t=2$, (b) $t=4.9$, (c) $t=28.6$.

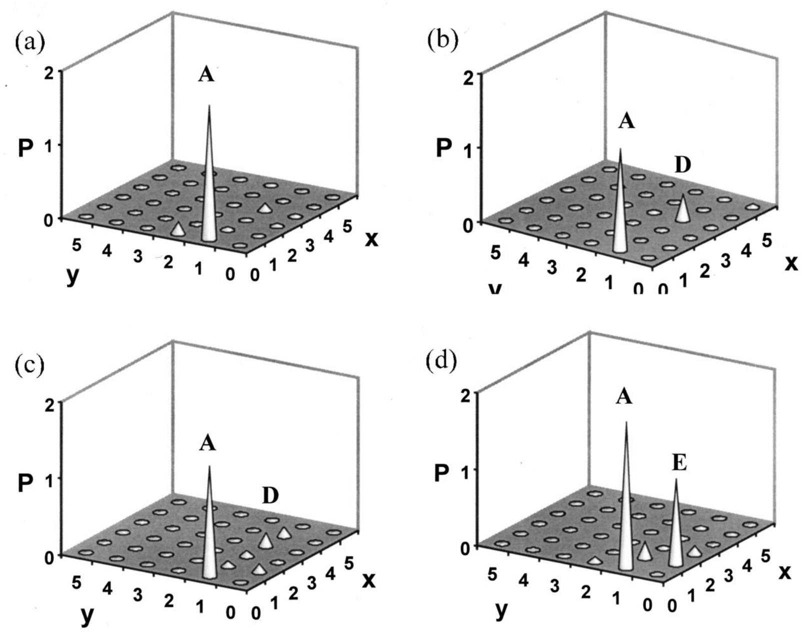

FIG. 16. Power spectrum density, P, of the transition from plug flow to a clump for a system with $L/W=4$, $W/d=33.3$, $\nu_{2\mathrm{d}}=0.31$, $e_p=0.85$, $e_w=0.97$, $\phi'=0.6$, $N_1=48$, and $N_2=12$. Cone plots of power spectrum at dimensionless times (a) $t=2$, (b) $t=7.5$, (c) $t=10$, (d) $t=28.8$. Corresponds to Figs. 5(a)–5(d).

plex), and the coordinates of **P** correspond to the harmonic values b_j and b_k. Due to the symmetry of **P** about the Nyquist frequency, half of the peak values for power in each of the x and y directions are redundant, and, as in Wang and Tong, only the first quadrant of the power matrix will be analyzed. Nonetheless, there is significant difficulty in distinguishing the nonconstant Fourier coefficients in the presence of large amplitude constant terms in each density function expansion. This problem is exacerbated since the amplitude of the constant term peak is 2× larger than all other peaks (except for the peak corresponding to the Nyquist frequency) due to symmetry properties. For this reason, the mean value of the density over the entire spatial domain in x and y was removed from the power spectra. This was achieved by setting the (0,0) coefficient of **X** to zero. (This simple filter was imposed after the FFT was executed instead of removing the mean before transforming, to avoid generating false coefficients from the resulting sharp discontinuities.)

The temporal development of the power spectra are depicted in Figs. 14–16 for systems corresponding to the parameters in Table I and increasing L/W ratios. The corresponding fully developed density waves can be seen in Fig. 3. Figure 14 depicts a system with $L/W=2$, simulated from the plug initial condition, and at dimensionless times corresponding to the scatter plots in Figs. 5(a) and 5(b). A dominant peak, labeled A, can be observed at wave number (0,1), where the first ordinate refers to the vertical direction, x. The transition from a plug to the one-humped wave is marked by the birth of a second peak B at (1,1), which grows to a maximum size and then remains almost constant as the one-humped wave structure reaches full development. For the $L/W=3$ case shown in Fig. 15, an equivalent behavior is observed [see Fig. 3(c) for the corresponding fully developed wave]. From the initial plug structure, where the (0,1) peak (Peak A) is dominant, the two-humped wave develops, which corresponds to the growth of a Peak C at (2,1). Similarly, the $L/W=4$ case in Fig. 16, is shown for dimensionless times corresponding to the scatter plots in Figs. 6(a)–6(d). The plug flow initial condition, with a peak at (0,1) transitions to a three-humped wave dominated by peak D at (3,1) [see Fig. 16(b)]. The transition to the clump condition corresponds to the appearance of a new peak E at (1,0), which eventually eclipses all other peaks except peak A at the larger time values.

Greater resolution in the wave number space and additional higher modes could be investigated by decreasing the interval size over which locally averaging is performed to generate the density data, although this would result in increased noise. In effect, this would increase the sampling frequency in the spatial domain. However, it should be noted that the additional resolution in the spatial domain would not result in greater resolution in the wave number space, but would only allow more of the higher frequency modes to become apparent. In Figs. 14–16, only the first six wave number ordinates in each direction were plotted. The other ordinates (totaling 12 in the W direction, and up to 48 in the L direction) are not shown due to: (i) The symmetry of the power spectrum around the Nyquist frequency, and (ii) the fact that the peaks of all other frequencies lower than the Nyquist frequency were negligible. Also, a common signal processing practice is to impose a window on the data to counter the effects of discretization when sampling the spatial domain, to reduce leakage of power amplitudes to the peaks of adjacent Fourier coefficients. In this case, windowing was deemed unsatisfactory since generation of false coefficients that fall off as $1/N_1$ and $1/N_2$ would be expected. As relatively few modes were expected, and the absolute magnitude of the power spectrum peaks are not as important as relative growth rates, the additional complexity of windowing was avoided.

The dominant frequency instability modes represented by peaks at (1,1), (2,1), and (3,1) represent antisymmetric density modes confined by the system dimensions. One could expect that for sufficiently long systems, the antisym-

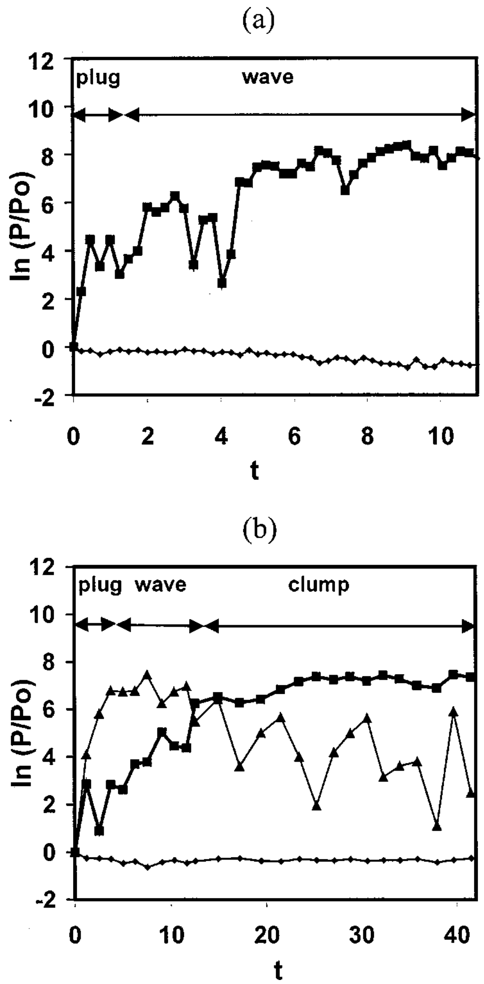

FIG. 17. Temporal evolution of Fourier modes for a system with $W/d=33.3$, $\nu_{2d}=0.31$, $e_p=0.85$, $e_w=0.97$, and $\phi'=0.6$. Plot of $\ln(P/P_0)$ for dominant modes against dimensionless time for (a) $L/W=2$, transition from plug to one-humped wave, -·- A (0,1), -■- B (1,1). (b) $L/W=4$, transition from plug to clump. -·- A (0,1), -▲- D (3,1), -■- E (1,0).

metric wave frequencies would occur at higher and higher frequencies in the x (or L) direction. Indeed for the case of $L/W=10$ [corresponding to Fig. 3(e)], Fourier analysis shows the dominance of a peak at (7,1), corresponding to a seven humped wave. This again collapses to a single clump at longer times, but not before two clumps become visible, and a peak of (2,0) is observed. However, this condition is not stable and eventually collapses to the one clump mode (0,1) as peak E dominates.

The transient development of each of the dominant frequency peaks identified above is tracked in Fig. 17. Wang and Tong[33] distinguished between linear and nonlinear growth of each mode in the continuum model using plots of $\ln(P/P_0)$, where P_0 is the initial amplitude of each power peak, and the same depiction is used here. In the present study, the amplitudes generally increase with time, except for the main lateral mode (0,1), which decreases as the central plug structure becomes less dominant for wavy and clumped flows. For the $L/W=2$ case shown in Fig. 17(a), growth of peak B to a plateau level marks the development of the stable S-shaped wave flow condition. Even at long times there is significant fluctuation (amplified by the log plot) of these modes due to the modulation of the wave as it moves through the channel. Similar trends are observed in the $L/W=3$ case (not shown). Turning to $L/W=4$ case shown in Fig. 17(b), peak A is at a maximum initially, when the plug flow is most pronounced. Peak D then starts to emerge as the three-humped wave forms. The log plot shows initial growth of this mode is relatively rapid, until the wavy flow is established, and growth terminates. The amplitude of the plug flow, peak A, remains fairly constant during this time, although a decrease can be seen at the establishment of the S-shaped wavy flow. To reach the clump flow at longer times, peak E at (1,0) grows before leveling off as the clump forms. It appears that the amplitude of the three-humped wave condition, peak D at (3,1), decreases correspondingly. At long times there is significant fluctuation in the (3,1) mode while the (1,0) mode levels off to a fairly constant value. The Fourier analysis was also applied to S-shaped waves and clumps for other parameter values, and similar results were observed.

IV. COMPARISON WITH THEORETICAL PREDICTIONS

We have shown using particle dynamic simulations that gravity flow of a granular material in a channel is not uniform but exhibits three distinct forms of inhomogeneities: A plug, an S-shaped wave and a clump. Wang *et al.*[30] investigated channel flow by examining the equations of motion for granular flow with constitutive relationships proposed by Lun *et al.*[32] and showed that density wave formation is a manifestation of a dynamical instability. They investigated both the (base) fully developed flow as well as the linear stability of these solutions to small perturbations. Plug flow was observed as the steady state, fully developed density profile. The base state was then found to be linearly unstable to perturbations in the form of density waves. Eigenfunctions corresponding to the unstable eigenvalues were also examined and these took the form of an antisymmetric traveling wave and two types of symmetric traveling waves. Wang and Tong[33] examined the temporal evolution of each individual mode through numerical simulation and Fourier analysis. The resulting density inhomogeneities they observed can be broadly classified within the categories of a plug, an S-shaped wave and a clump (although they were not discussed in this way). In this section a direct comparison of the density waves from our particle dynamics simulations and the linear stability analysis of Wang *et al.*[30] and the numerical simulation of Wang and Tong[33] will be discussed. It should be noted that their analyses considered a three-dimensional system in which the motion of the particles was confined to a two-dimensional (2D) plane. A comparison between the three-dimensional (3D) theoretical stability analysis and the two-dimensional results presented in this work can be accomplished by a conversion of the solids fraction. The conversion, which we used in this work, was derived based on a comparison between a hexagonal lattice and an FCC unit cube[55] and can be expressed as

$$\varepsilon_{3D} = 1 - \frac{2}{\sqrt{\pi\sqrt{3}}}(1-\varepsilon_{2D})^{3/2} \tag{12}$$

where ε is the void fraction and is equal to $1-\nu$.

We carried out simulations for the same particle diameter, density and specularity coefficient as in the continuum stability analysis and numerical simulation. They examined a range of system parameters including W/d, solids fraction, and coefficient of restitution of the particles and coefficient of restitution of the walls. They found that the coefficient of restitution for collisions between particles and walls had little effect on the overall flow behavior, as was observed in this work. Their study examined three systems in detail including a system with a $W/d=66$, three-dimensional solids fraction of $\nu_{3D}=0.15$, $e_p=0.95$, $\phi'=0.6$, and $e_w=0.97$. For this set of parameters, they observed that the base plug flow is unstable to both symmetric and antisymmetric density waves. The dominant instability occurs at a wavelength of 1.3 times the width of the system and is an antisymmetric instability; the addition of the density eigenfunction to the base (plug flow) state would appear to result in a flow structure similar to the one-humped wavy flow observed in Fig. 3(b) [see Fig. 14(f) of Ref. 30 and Fig. 12 of Ref. 33]. (It should be noted that Wang *et al.*[30] and Wang and Tong[33] plot two vertical periods of their periodic box. In addition the waves presented by Wang and Tong[33] are stretched in the vertical direction and plotted in square boxes.)

One would expect to observe the dominant instability in systems that are larger than the wavelength of the dominant instability. For this set of parameters, the wavelength of the symmetric instability is larger than the dominant wavelength and therefore would not be manifested in this system; the addition of the symmetric density eigenfunction to the base (plug flow) state would appear to result in a flow structure similar to a clump. These results indicate that in simulations with L/W greater than 1.3 we would expect to find antisymmetric density waves (assuming that nonlinear effects do not completely change the structure of the waves predicted by their analysis). This is born out by our numerical experiments where we indeed do observe an antisymmetric instability (see Fig. 18) although exact quantitative agreement is not observed (as discussed below). Wang and Tong investigated the Fourier modes of this antisymetric density wave instability,[33] and observe two series of peaks. The series that grows initially (also the linear instability) correspond to the peaks A-B discussed above (in Sec. III C). Wang and Tong also see all of the A peaks of the series cede to a new set of peaks. Although the discreteness inherent in this particle dynamic simulation does not afford the same resolution as the Fourier transforms in the continuum study, the investigations in frequency space do add support that both simulations generate the same phenomena.

Figure 18 shows the fully developed state for our simulations with equivalent parameters to the continuum study; $W/d=66$, $\nu_{2D}=0.31$ (equivalent of $\nu_{3D}=0.15$), $e_p=0.95$, $\phi'=0.6$, and $e_w=0.97$. This figure shows that when the $L/W=0.5$ the system is stable and flows as a plug. As the size of the system increases and $L/W=2$ the system be-

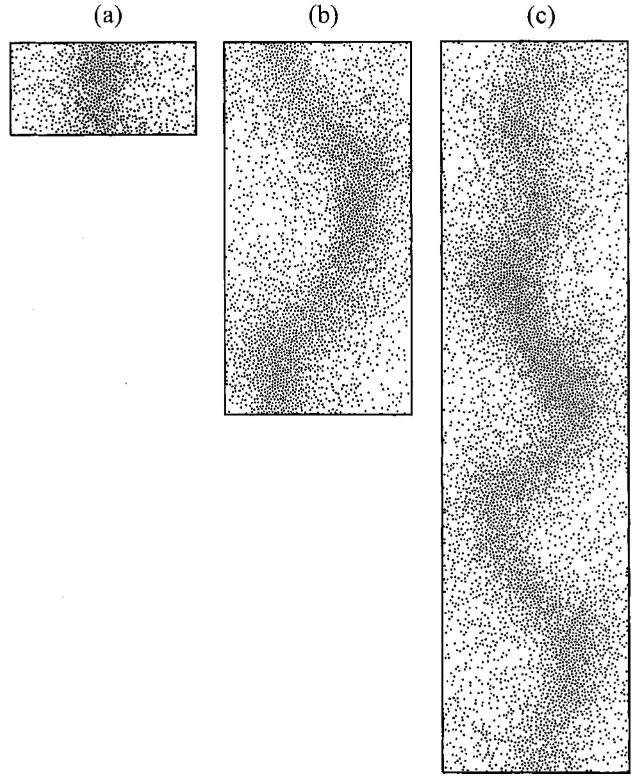

FIG. 18. Scatter plots of the position of the particles at statistical steady state for systems of varying size. $W/d=66$, $\nu_{2d}=0.31$, $e_p=0.95$, $e_w=0.97$, and $\phi'=0.6$. (a) $L/W=0.5$, (b) $L/W=2$, (c) $L/W=4$.

comes unstable to fluctuations in the vertical direction and a one-humped wave is apparent. For even larger systems, $L/W=4$, a two-humped antisymmetric instability is observed and this develops into a two-humped density wave. The growth of two (and more) humped waves can be understood from (and are in accord with) the linear stability results of Wang *et al.*[30] They considered the fate of only single-humped modes but they employed periodic boundary conditions in the vertical direction; this means that any results for a one-humped mode in a channel of length L will be the same as those for the corresponding two-humped mode in a channel of $2L$ and a three-humped mode in a channel of $3L$, and so on. They observe the maximum growth rate (for single-humped modes) at $L=1.3\,W$. Thus there also exists a two-humped mode in channel of $L=2.6\,W$ (twice the original length) which would develop at this same maximum growth rate. Thus by the very fact that the maximum growth rate is at $L=1.3\,W$, one can conclude that the growth rate of a single-humped mode in a channel of $L=2.6\,W$ will be less than the growth rate of the two-humped mode in this channel. This same argument holds for channel lengths than are not multiples of that corresponding to the maximum growth rate. Thus, the linear stability results also explain the observation that in systems of large lengths we observe the initial development of many-humped S-shaped waves (see Sec. III A). As it turns out these many-humped waves later go on to coalesce to form a clump but this can be interpreted as a result of nonlinear effects (which cannot be captured by the linear stability analysis). We note, that while Wang and

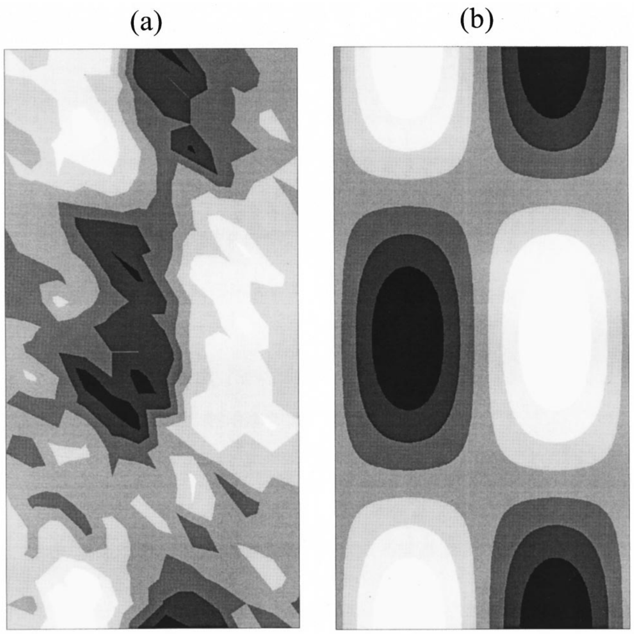

FIG. 19. Contour plot of a system at statistical steady state with $L/W=2$, $W/d=66$, $\nu_{2d}=0.31$, $e_p=0.95$, $e_w=0.97$, and $\phi'=0.6$. (a) Locally averaged eigenfunctions, (b) $z=A\sin(x)\sin(y)$.

Tong[33] did capture nonlinear effects in their simulations, they only examined the fate of one-humped disturbances.

For the above-mentioned case there is qualitative agreement between the particle dynamic simulations and the linear stability analysis in that the basic structures we observe can be inferred from the linear stability analysis, although exact quantitative agreement for a given parameter value is not observed. Perhaps this is not surprising given the uncertainties with the conversion of the volume fractions. In addition, as discussed by Wang *et al.*,[30] the equations of motion used in their work were derived with the assumption that the coefficient of restitution differs only slightly from unity.

In any event, a linear analysis only predicts the direction of growth of instabilities and is only valid near the steady solution. A more instructive comparison would be to compute (the equivalent of) eigenfunctions directly from our simulations and compare those results with the eigenfunctions presented by Wang *et al.*[30] This was accomplished by using a fully developed plug flow state as the initial condition for a larger system that (we know) will become unstable to density waves. As expected a density wave started to develop and a snapshot of this low amplitude wave was taken. A contour plot of the density distribution of the plug flow state was subtracted from the contour plot of the low amplitude wave to construct a density "eigenfunction." This eigenfunction is shown for $L/W=2$ in Fig. 19(a). Although the contours represented in these figures are not smooth curves, due to the discrete nature of the simulations, the antisymmetric one-humped instability, discussed above, is apparent from this plot. The corresponding Fourier analysis of this system shows that the dominant Fourier mode is $\sin(x)\sin(y)$; this Fourier mode (with a vertical phase shift) is plotted in Fig. 19(b). This Fourier mode was computed earlier as Peak B (1,1) for the $L/W=2$ case. The computed mode in Fig. 19 strongly resembles the eigenfunction plot shown in Fig. 14(f) of Wang *et al.*[30] It is also of interest to compare the wave velocities that the continuum work predicts with those we observe. For $L/W=2$ we compute a dimensionless wave velocity for the S-shaped wave of 7.7 ± 1.6 while Wang *et al.*[30] compute a phase velocity of 10.8 corresponding to the maximum growth rate.

Wang *et al.*[30] also considered a system with a $W/d=33.3$, $\nu_{3D}=0.15$, $e_p=0.95$, $\phi'=0.6$ and $e_w=0.97$. (This system has material properties equivalent to the two-dimensional system listed in Table I but with an increased value of e_p.) They found that the base plug flow is only unstable to symmetric density waves; the addition of the density eigenfunction to the base (plug flow) state would result in a flow structure similar to the clump observed in Fig. 3(d) [see Fig. 14(b) of Ref. 30 and Fig. 7 of Ref. 33]. Simulations of systems with the same parameters as this system (using $\nu_{2D}=0.31$ which is equivalent to $\nu_{3D}=0.15$) for L/W as large as 20 showed a plug flow and did not exhibit clump formation. The lack of agreement in this system is most likely due to the conversion between two and three-dimensional systems.

Although Wang *et al.*[30] do not report results for a system equivalent to the two-dimensional system listed in Table I, the solution for $e_p=0.85$ would only change quantitatively from $e_p=0.95$. From their results for $e_p=0.95$, it is apparent that the instability with the highest growth rate can either be a symmetric or an antisymmetric density wave depending on the wavelength of the instability (although the highest growth rate is negative for wavelengths smaller than 6.28 and, therefore, only symmetric density waves have positive growth rates). The transition from the antisymmetric instability to the symmetric instability occurs at a wavelength of 3.92. We can now suggest how these results will change as e_p is decreased. Decreasing e_p tends to make the system less stable and results in an increase of the growth rate of an instability at a particular wavelength. Instabilities that previously had negative growth rates could have a positive growth rate at lower e_p. It is possible that a system with a lower value of e_p has negative growth rates for small wavelengths. Then at some wavelength smaller than the transition from antisymmetric to symmetric instabilities the growth rate would be positive and antisymmetric density waves would manifest. As the wavelength is increased there would then be a transition, above which the symmetric instability would occur. This is indeed what we found and presented in Fig. 3. These simulations show that for small systems the flow is stable and exists as a plug. As the size of the system is increased the system becomes unstable to fluctuations in the vertical direction and wavy flow is apparent. When L/W is further increased symmetric instabilities are manifested by the appearance of a clump. However even in this case there is an important difference: Wang *et al.*[30] and Wang and Tong[33] show results where the only unstable mode is a symmetric traveling wave. In such a case the instability of the plug takes the form of a symmetric wave that develops into a clump that moves through the system. While we have carried out hundreds of simulations for a large range of parameter values we have never seen a purely symmetric instability act on the plug. Instead we always observe the presence of an antisymmetric mode at short times. For systems of large L/W the symmetric mode does come into play (as discussed above) and as time progresses it even dominates; and a fully developed clump state is observed (see Fig. 5). At the same time, we should note that the inherent noise in the MD simulations and the difficulty in separating linear and nonlinear effects means that we cannot rule out that the *linear instability* is purely symmetrical for some of the runs. We should also point out that our results do not rule out the possibility of parameter ranges existing where the purely symmetric mode dominates. In any event it is of interest to compare the wave velocities we observe for a clump with those computed in the continuum analysis (taking into account that the e_p values are different). For the clump in Fig. 3(d) we computed a wave velocity of 9.0 ± 0.8 while Wang *et al.*[30] compute a phase velocity of 7.2 corresponding to the maximum growth rate.

We are unable to compare our results with the third system examined by Wang *et al.*[30] because it is an extremely dense system and the (equivalent) simulation used for this study experiences inelastic collapse.[56] In summary Wang *et al.*[30] and Wang and Tong[33] observe a base plug flow state and instabilities that take the form of antisymmetric or symmetric density waves. We do qualitatively observe the base state and the types of instabilities predicted by the linear stability analysis. Morevoer both the continuum analysis and molecular-dynamic simulations lead to traveling density waves that can be characterized as S-shaped waves or clumps. However, for the parameter values we examined the results do not agree quantitatively. Once again, this could be due to the conversion between two and three-dimensional systems resulting in inaccurate values of solids fraction; the lack of agreement could also arise from the inherent assumption in the continuum equations that the coefficient of restitution differs only slightly from unity.

V. CONCLUSIONS

The formation of density inhomogeneities during gravity driven flow of granular material in a channel has been examined. Three distinct steady state forms of inhomogeneities have been observed. A parametric study identified the important system parameters and how they affected the type of inhomogeneity which is observed. It was found that a variation in system and particle properties can significantly affect the formation of density waves but the wall properties we considered had little effect. The effect of density variations within the flow domain on global system properties was analyzed, and the temporal evolution of characteristic Fourier coefficients was quantified. It was found that density waves could significantly change flow properties such as stresses, pressures, and granular temperature. Finally, simulation results were then compared with the theoretical results of Wang *et al.*[30] and Wang and Tong[33] and fairly good qualitative agreement was found for the types of instabilities and density waves that were observed.

Particle dynamic simulations have provided an ideal means of testing continuum theories derived from the kinetic theory of dense gases.[3,10,20] For channel flow, further continuum and particle dynamic work is needed in order to afford a definitive comparison. Moreover, continuum theories assume that there is scale separation between properties of the flow that are of the scale of grains (microscopic) and global system properties (macroscopic). It is inherent to these models that there are length scales above which system properties can be averaged. In general, density wave formation directly affects the flow properties of the system. Systems must therefore be modeled either at scales which capture structure formation or coarse-grid models must include corrections which account for the additional effects of inhomogeneities. Work on coarse-grid models has been initiated for gas–particle flows.[57] The prevalence of inhomogeneities in granular flows suggests that coarse-grid models may be appropriate for granular flows.

ACKNOWLEDGMENTS

This work has been partially supported by the National Science Foundation and the National Aeronautics and Space Administration. We would like to acknowledge the assistance of Clay Sutton.

[1] J. T. Jenkins and M. W. Richman, ''Plane simple shear of smooth inelastic circular disks: the anisotropy of the second moment in the dilute and dense limits,'' J. Fluid Mech. **192**, 313 (1988).
[2] C. S. Campbell, ''Rapid granular flows,'' Annu. Rev. Fluid Mech. **22**, 57 (1990).
[3] O. R. Walton, H. Kim, and A. D. Rosato, ''Microstructure and stress differences in shearing flows,'' in *Mechanics Computing in 1990's and Beyond*, edited by H. Adeli and R. Sierakowski (ASCE, New York, 1992).
[4] I. Goldhirsch and N. Sela, ''Origin of normal stress differences in rapid graular flows,'' Phys. Rev. E **54**, 4458 (1996).
[5] H. M. Jaeger, S. R. Nagel, and R. P. Behringer, ''The physics of granular materials,'' Rev. Mod. Phys. **68**, 1259 (1996).
[6] W. L. Vargas and J. J. McCarthy, ''Heat conduction in granular materials,'' AIChE J. **47**, 1052 (2001).
[7] C. S. Campbell and C. E. Brennen, ''Chute flows of granular materials some computer simulations,'' J. Appl. Mech. **52**, 172 (1985).
[8] K. Hui and P. K. Haff, ''Kinetic grain flow in a vertical channel,'' Int. J. Multiphase Flow **12**, 289 (1986).
[9] M. A. Hopkins and M. Y. Louge, ''Inelastic microstructure in rapid granular flows of smooth disks,'' Phys. Fluids A **3**, 47 (1991).
[10] B. E. Sanders and N. L. Ackerman, ''Instability in simulated granular chute flow,'' J. Eng. Mech. **117**, 2396 (1991).
[11] I. Goldhirsch and G. Zanetti, ''Clustering instability in dissipative gases,'' Phys. Rev. Lett. **70**, 1619 (1993).
[12] I. Goldhirsch, M.-L. Tan, and G. Zanetti, ''A molecular dynamical study of granular fluids I: The unforced granular gas in two dimensions,'' J. Sci. Comput. **8**, 1 (1993).
[13] R. Gudhe, R. C. Yalamanchili, and M. Massoudi, ''Flow of granular materials down a vertical pipe,'' Int. J. Non-Linear Mech. **29**, 1 (1994).
[14] L. S. Mohan, P. R. Nott, and K. K. Rao, ''Fully developed flow of coarse granular materials through a vertical channel,'' Chem. Eng. Sci. **52**, 913 (1997).
[15] J. C. Chen, ''Clusters,'' in *Progress in Fluidized and Fluid Particle Systems*, edited by D. King (American Institute of Chemical Engineers, New York, 1996).
[16] S. Dasgupta, R. Jackson, and S. Sundaresan, ''Turbulent gas–particle flow in vertical risers,'' AIChE J. **40**, 215 (1994).
[17] C. M. Hrenya and J. L. Sinclair, ''Effects of particle-phase turbulence in gas–solid flows,'' AIChE J. **43**, 853 (1997).
[18] M. S. Detamore, M. A. Swanson, K. R. Frender, and C. M. Hrenya, ''A kinetic theory analysis of the scale-up of circulating fluidized beds,'' Powder Technol. **116**, 190 (2001).
[19] E. D. Liss and B. J. Glasser, ''The influence of clusters on the stress in a sheared granular material,'' Powder Technol. **116**, 116 (2001).

[20]C. S. Campbell and A. Gong, ''The stress tensor in a two-dimensional granular shear flow,'' J. Fluid Mech. **164**, 107 (1986).
[21]O. R. Walton and R. L. Braun, ''Stress calculations for assemblies of inelastic spheres in uniform shear,'' Acta Mech. **63**, 73 (1986).
[22]C. S. Campbell, ''The stress tensor for simple shear flows of a granular material,'' J. Fluid Mech. **203**, 449 (1989).
[23]S. B. Savage and R. Dai, ''Studies of granular shear flows wall slip velocities, 'layering,' and self-diffusion,'' Mech. Mater. **16**, 225 (1993).
[24]C. K. K. Lun and A. A. Bent, ''Numerical simulation of inelastic frictional spheres in simple shear flow,'' J. Fluid Mech. **258**, 335 (1994).
[25]B. E. Sanders and N. L. Ackerman, ''Microstructures in rapid gravity channel flow,'' in *Advances in Micromechanics of Granular Materials*, edited by H. H. Shen, M. Satake, M. Mehrabadi, C. S. Chang, and C. S. Campbell (Elsevier Science, Amsterdam, 1992).
[26]J. Lee and M. Leibig, ''Density waves in granular flow: A kinetic wave approach,'' J. Phys. I **4**, 507 (1994).
[27]T. Poschel, ''Recurrent clogging and density waves in granular material flowing through a narrow pipe,'' J. Phys. I **4**, 499 (1994).
[28]G. Peng and H. J. Herrmann, ''Density waves of granular flow in a pipe using lattice-gas automata,'' Phys. Rev. E **49**, R1796 (1994).
[29]T. Riethmuller, L. Shimansky-Geier, D. Rosenkranz, and T. Poschel, ''Langevin equation approach to granular flow in a narrow pipe,'' J. Stat. Phys. **86**, 421 (1997).
[30]C.-H. Wang, R. Jackson, and S. Sundaresan, ''Instabilities of fully developed rapid flow of a granular material in a channel,'' J. Fluid Mech. **342**, 179 (1997).
[31]A. Valence and T. Le Pennec, ''Nonlinear dynamics of density waves in granular flows through narrow vertical channels,'' Eur. Phys. J. B **5**, 223 (1998).
[32]C. K. K. Lun, S. B. Savage, D. J. Jeffrey, and N. Chepurniy, ''Kinetic theories for granular flow: Inelastic particles in Couette flow and slightly inelastic particles in a general flow field,'' J. Fluid Mech. **140**, 223 (1984).
[33]C.-H. Wang and Z. Tong, ''On the density waves developed in gravity channel flows of granular materials,'' J. Fluid Mech. **435**, 217 (2001).
[34]S. Horikawa, A. Nakahara, T. Nakayama, and M. Matsushita, ''Self-organized critical density waves of granular material flowing through a pipe,'' J. Phys. Soc. Jpn. **64**, 1870 (1995).
[35]J. P. Raafat, J. P. Hulin, and J. P. Herrmann, ''Density waves in dry granular media falling through a vertical pipe,'' Phys. Rev. E **53**, 4345 (1996).
[36]O. Moriyama, N. Kurowa, M. Kanda, and M. Matsushita, ''Dynamics if granular flow through a vertical pipe: Effect of medium flow,'' J. Phys. Soc. Jpn. **67**, 1616 (1998).
[37]J.-L. Aider, N. Sommier, T. Raafat, and J.-P. Hulin, ''Experimental study of a granular flow in a vertical pipe: A spatiotemporal analysis,'' Phys. Rev. E **59**, 778 (1999).
[38]J. Hua and C.-H. Wang, ''Electrical capacitance tomography measurements of gravity-driven granular flows,'' Ind. Eng. Chem. Res. **38**, 621 (1999).
[39]J. A. Yasuna, H. R. Moyer, S. Elliott, and J. L. Sinclair, ''Quantitative predictions of gas–particle flow in a vertical pipe with particle–particle interactions,'' Powder Technol. **84**, 23 (1995).
[40]C. K. K. Lun and S. B. Savage, ''A simple kinetic theory for granular flow of rough, inelastic, spherical particles,'' J. Appl. Mech. **54**, 47 (1987).
[41]P. C. Johnson, P. Nott, and R. Jackson, ''Frictional-collisional equations of motion for particulate flows and their application to chutes,'' J. Fluid Mech. **210**, 501 (1990).
[42]D. C. Rapaport, ''Large-scale molecular dynamics simulation using vector and parallel computers,'' Comput. Phys. Rep. **9**, 1 (1988).
[43]M. Nakagawa and T. Imaizumi, ''Simulations of rapid bimodal granular flows,'' in *Advances in Micromechanics of Granular Materials*, edited by H. H. Shen, M. Satake, M. Mehrabadi, C. S. Chang, and C. S. Campbell (Elsevier Science, Amsterdam, 1992).
[44]C. K. K. Lun, ''Granular dynamics of inelastic spheres in Couette flow,'' Phys. Fluids **8**, 2868 (1996).
[45]X. M. Zheng and J. M. Hill, ''Boundary effects for Couette flow of granular materials: Dynamical modelling,'' Appl. Math. Model. **20**, 82 (1996).
[46]M. Alam and P. R. Nott, ''The influence of friction on the stability of unbounded granular shear flow,'' J. Fluid Mech. **343**, 267 (1997).
[47]A. Karion and M. L. Hunt, ''Wall stresses in granular Couette flows of monosized particles and binary mixtures,'' Powder Technol. **109**, 45 (2000).
[48]C.-H. Wang, R. Jackson, and S. Sundaresan, ''Stability of bounded rapid shear flows of a granular material,'' J. Fluid Mech. **308**, 31 (1996).
[49]E. D. Liss, ''The effect of microstructure on the flow of granular materials: simple shear and gravity driven flow,'' Ph.D. thesis, Chemical and Biochemical Engineering, Rutgers University (2001).
[50]A. D. Rosato and H. Kim, ''Particle dynamics calculations of wall stresses and slip velocities for Couette flow of smooth inelastic spheres,'' Continuum Mech. Thermodyn. **6**, 1 (1994).
[51]B. J. Glasser and I. Goldhirsch, ''Scale dependence, correlations and fluctuations in rapid granular flows,'' Phys. Fluids **13**, 407 (2001).
[52]B. Miller, C. O'Hern, and R. P. Behringer, ''Stress fluctuations for continuously sheared granular materials,'' Phys. Rev. Lett. **77**, 3110 (1996).
[53]C. S. Campbell, ''Impulse strengths in rapid granular shear flows,'' Acta Mech. **104**, 65 (1994).
[54]C.-H. Wang and Z. Tong, ''Transient development of instabilities in bounded shear flow of granular materials,'' Chem. Eng. Sci. **53**, 3803 (1998).
[55]B. P. B. Hoomans, J. A. M. Kuipers, W. J. Briels, and W. P. M. Van Swaaij, ''Discrete particle simulation of bubble and slug formation in a two-dimensional gas-fluidised bed: A hard sphere approach,'' Chem. Eng. Sci. **51**, 99 (1996).
[56]M. Alam and C. M. Hrenya, ''Inelastic collapse in simple shear flow of a granular medium,'' Phys. Rev. E **63**, 061308 (2001).
[57]K. Agrawal, P. N. Loezos, M. Syamlal, and S. Sundaresan, ''The role of mesoscale structures in rapid gas–solid flows,'' J. Fluid Mech. **445**, 151 (2001).